

# Detecting compact dark matter in galaxy clusters via gravitational microlensing: A2218 & A370

A.V. Tuntsov<sup>1</sup>\*, G.F. Lewis<sup>1</sup>†, R.A. Ibata<sup>2</sup>‡ & J.-P. Kneib<sup>3</sup>§,

<sup>1</sup>*A29, School of Physics, University of Sydney, NSW 2006, Australia*

<sup>2</sup>*Observatoire de Strasbourg, 11, rue de l’Université, F-67000, Strasbourg, France*

<sup>3</sup>*Observatoire Midi-Pyrénées, 14 Av. E. Belin, 31400 Toulouse, France*

*on leave at Caltech, Astronomy, 105-24, Pasadena, CA 91125, USA*

Accepted 2004 June 10. Received 2004 June 8; in original form 2004 March 31

## ABSTRACT

After decades of searching, the true nature of dark matter still eludes us. One potential probe of the form of dark matter in galaxy clusters is to search for microlensing variability in the giant arcs and arclets. In this paper, a simple method is introduced to characterize pixel variability in the limit of high optical depth to microlensing. Expanding on earlier work, the expected microlensing signal for two massive clusters, A2218 & A370 is calculated. It is found that the microlensing signal depends sensitively upon the mix of smooth and compact dark matter in the cluster. Comparison of two deep exposures taken with *James Webb Space Telescope* or two hour long exposures taken with a 30-metre class telescope in two epochs separated by a few years will possibly detect about a few dozen pixels which show strong variability due to microlensing at  $5\sigma$  level, revealing wealth of information on the microlensing population.

**Key words:** gravitational lensing : microlensing : high optical depth – dark matter : compact – galaxies : clusters : individual (A370, A2218)

## 1 INTRODUCTION

There is significant evidence that most of the energy density in the Universe resides in the forms yet unknown, but the physical nature of this dark matter is an issue of live debate and is far from being understood (Lahav & Liddle 2003; Muñoz 2003). Typical explanations invoke either compact objects, such as primordial black holes, stellar remnants or planets, or continuous material such as weakly interacting massive particles, unseen hydrogen or more exotic explanations. Potential clues to the nature of dark matter have recently been uncovered with the detection of neutrino mass and observations of compact massive objects thought to be mostly white dwarfs in Galactic neighbourhood (e.g., Fukuda et al. 2000; Alcock et al. 2000). However, given their mass neutrinos cannot contain more than  $\sim 13$  per cent of the dark matter mass budget (Hu, Eisenstein & Tegmark 1998). Furthermore, the halo microlensing programs constrain compact objects in the mass range of  $(10^{-7} - 10^{-1})M_{\odot}$  to making no more than 10 per cent of the Galactic halo (Sadoulet 1999).

Gravitational lensing has allowed the detailed reconstruction of the projected mass distribution in galaxy clusters (e.g., Ebbels et al. 1998). Unfortunately such analysis does not probe the fundamental nature of dark matter. However, although deflection angles due to compact objects in the dark matter are negligible their derivatives may be substantial which means that although the granularity of dark matter cannot change the morphology of lensed systems, this *microlensing* can have significant impact on the observed fluxes (Liebes 1964; Paczyński 1986). As the mutual configuration of sources and lenses change with time, this results in variability of the observed flux.

Several microlensing programs have been proposed and undertaken, the most successful of them being the microlensing experiments towards Galactic bulge and Magellanic Clouds by MACHO, EROS and OGLE collaborations (Alcock et al. 2000; Lasserre et al. 2000; Udalski, Kubiak & Szymanski 1997). Another approach is pixel lensing when the search focuses not on individual sources but on a large number of stars seen as a single pixel of the image. Events of strong lensing of a single star can be detected in the pixel light though they never dominate it. Such events have been discussed in connection with the galaxies M31 and M87 (Crotts 1992; Baillon et al. 1993; Gould 1995), and a few observational programs monitoring these

\* E-mail:tyomich@physics.usyd.edu.au

† E-mail: gfl@physics.usyd.edu.au

‡ E-mail: ibata@pleiades.u-strasbg.fr

§ E-mail: kneib@ast.obs-mip.fr

galaxies have been implemented (Crotts & Tomaney 1996; Ansari et al. 1997; Riffeser et al. 2001; Baltz et al. 2003).

Further away from the Galaxy, it has been proposed to search for microlensing-induced variability of quasars seen through galaxy clusters (Walker & Ireland 1995; Tadros, Warren & Hewett 1998). This has been undertaken for the Virgo cluster, although its close proximity ensures that the optical depth to microlensing is low. Although analysis of the quasar variability based on a long observation series by Hawkins (1996) let him conclude that the dark matter may be dominated by Jupiter-mass microlenses, this idea is not widely supported. One of the difficulties here is that quasars are expected to possess intrinsic variability (Zackrisson et al. 2003) which significantly complicates microlensing studies. Totani (2003) proposed to explore the advantage of the recent discovery of a galaxy cluster found just behind the rich cluster Abell 2152 but this has yet to result in an observational program.

Another possibility is to look for the variations in surface brightness of strongly lensed distant galaxies – e.g., giant gravitationally lensed arcs (Lewis & Ibata 2001; Lewis, Ibata & Wyithe 2000). They are found in the regions of large magnification and therefore high optical depth. Assuming that microlenses make up an appreciable fraction of the lensing mass, it means that in any instant all the stars in a pixel are subject to strong microlensing and therefore an investigation of the surface brightness variability is effectively reduced to an investigation of the behaviour of the sum of a large number of individual fluxes with fairly well known individual statistical properties.

This study extends the analysis of Lewis et al. (2000) and provides a general method for the analytic calculation of variability patterns given the convergence and shear values. We apply it to the two well-studied galaxy clusters – Abell 370 and Abell 2218. In the next section we describe and justify the method we use, and then calculate the value of individual microlensing-induced variability dispersion as a function of standard microlensing parameters. Section 3 discusses observational prospects for detecting this sort of variability. We discuss our results in section 4.

## 2 GENERAL METHOD

### 2.1 Statistical approach

The goal of this section is to learn to characterize the variability in pixels of images of distant galaxies with a few parameters. We show that the high optical depth and large numbers of stars forming the pixel allow one to reduce this to a single parameter – dispersion – as the observed flux distribution can be approximated by the Gaussian function with good accuracy.

The major assumption we make in our investigation is that the fluxes of individual stars, which vary as stars and lenses move with respect to each other, do so independently. This is a natural assumption since individual stars in the source plane are distributed in a random manner. It might be worth considering the presence of some form of agglomerations in pixels but this seems to be an unnecessary complication at the present stage.

We consider statistical properties ‘as static’ – i.e. on

time scales greater than typical individual variability scale given by the time of Einstein-Chwolson radius crossing ( $r_e/v$ ), and therefore are interested in the probability distribution function of the summed pixel flux. The typical fluxes in pixels forming images of strongly lensed galaxies correspond to the range in luminosity of thousands to billions of solar luminosities – and therefore contain very large numbers of stars. This fact along with the variability independence immediately suggests using the central limit theorem to infer the statistical properties of the pixel flux.

Indeed, let the intrinsic (unlensed) fluxes of the pixel population stars be  $\{L_i\}$ ,  $i = 1..N$ ,  $N$  being the number of stars in the pixel. If we neglect the fraction of stars intrinsically variable at the same level and time scale as the variability caused by the microlensing, the role of  $L_i$  is to normalize the variability in magnification factor  $\mu_i$  arising as the source stars move through the magnification map:

$$L_i^{obs} = L_i \mu_i \quad (1)$$

and  $\mu_i$  can be considered a random variable.

The probability distribution of  $\mu_i$  does depend on the individual characteristics of the source – mostly, the size of its disc. However, as we will see in the following section, this dependence is not strong and, to show the validity of Gaussian approximations it is enough to assume that  $\mu_i$  distribution is identical for all  $i$  and only depends on (macro) lensing parameters in the pixel.<sup>1</sup>

The flux observed in the pixel is given by

$$L^{obs}|_{\{L_i\}} = \sum_{i=1}^N L_i \mu_i \quad (2)$$

and its average value is

$$\overline{L^{obs}}|_{\{L_i\}} = \overline{\mu} \sum_{i=1}^N L_i, \quad (3)$$

where the bar denotes the averaging over the lensing configuration at a given convergence and shear (assuming a sort of ergodic hypothesis this is equivalent to averaging over time).

Let us define  $\delta L_i \equiv (\mu_i - \overline{\mu}) L_i$  and consider the deviation of  $L^{obs}|_{\{L_i\}}$  from its average value:

$$\delta L|_{\{L_i\}} = \sum_{i=1}^N L_i (\mu_i - \overline{\mu}) \quad (4)$$

Let us also define the second and third moments of the distribution in  $\mu$ :  $\sigma_\mu^2 \equiv \overline{(\mu - \overline{\mu})^2}$  and  $\beta \equiv \overline{(\mu - \overline{\mu})^3}$ . Clearly, the corresponding moments for  $\delta L_i$  equal  $L_i^2 \sigma_\mu^2$  and  $L_i^3 \beta$ .

According to Lyapunov theorem, the actual probability distribution function  $F$  of  $\delta L|_{\{L_i\}}$  tends to the Gaussian approximation

$$\Phi(\delta L) = \frac{1}{\sqrt{2\pi\sigma^2}} e^{-\frac{\delta L^2}{2\sigma^2}} \quad (5)$$

where we dropped  $\{L_i\}$  subscript for clarity, with

$$\sigma^2 \equiv \sigma_\mu^2 \sum_i L_i^2 \quad (6)$$

<sup>1</sup> We also assume that these parameters are constant throughout the pixel and this is a natural assumption in most cases.

The accuracy of this approximation in Kolmogorov ( $L_\infty$ ) measure  $\rho(F, \Phi) \equiv \sup_{x \in \mathcal{R}} |F(x) - \Phi(x)|$  is not worse than  $cA$ , where

$$A \equiv \frac{\beta}{\sigma_\mu^3} \frac{\sum L_i^3}{(\sum L_i^2)^{3/2}} \quad (7)$$

(Berry 1941; Esseen 1942) and  $c \equiv \frac{\sqrt{10}+3}{6\sqrt{2\pi}} \approx 0.41$  (Chistyakov 2001).

Although the value of the second fraction in  $A$  may, depending on  $\{L_i\}$ , be as large as unity its typical value is of order  $\langle L_i^3 \rangle / (\langle L_i^2 \rangle^{3/2} \sqrt{N})$ , where the angled brackets denote averaging over the luminosity function (which, up to a distance- and band-dependent constant, is the distribution of intrinsic fluxes).

With the luminosity function given by Jahreiss & Wielen (1997)<sup>2</sup>,  $\langle L_i^3 \rangle \approx 10^3 L_\odot^3$  and  $\langle L_i^2 \rangle \approx 10 L_\odot^2$ , therefore

$$cA \approx 10 \frac{\beta}{\sigma_\mu^3} \frac{1}{\sqrt{N}}. \quad (8)$$

To estimate the values of  $\beta$  and  $\sigma_\mu$  it is sufficient to use a rather coarse ‘model’ probability distribution density  $p(\mu)$  which is normalized to unity and has three basic properties established theoretically:

- (i)  $p(\mu) = 0$  at  $\mu \leq 1$
- (ii)  $\int d\mu p(\mu) \mu = \mu_{th}$ ,  $\mu_{th} = |(1 - \kappa^2) - \gamma^2|^{-1}$
- (iii)  $p(\mu) \sim \mu^{-3}$  at  $\mu \gg 1$ .

The job is done by the following ‘model’  $p(\mu)$ :

$$p(\mu) = \frac{2(\mu_o - 1)^2(\mu - 1)}{[(\mu - 1)^2 + (\mu_o - 1)^2]^2}. \quad (9)$$

The second condition implies  $\mu_o - 1 = 2(\mu_{th} - 1)/\pi$ .

This distribution does not possess the second moment, let alone the third, as a result of the (iii) property. However, the finite size of the source places a cut-off  $\mu_{max}$  at the high values of  $\mu$  (for a single point mass  $\mu_{max}$  is nearly inversely proportional to the source size as was shown by Liebes (1964)). Since  $\mu_{max} \gg \mu_o$  it does not affect either norm or the first moment and therefore with  $\sigma_\mu^2 \approx 2\mu_o^2 \ln(\mu_{max}/\mu_o) \approx \mu_{th}^2 \ln(\pi\mu_{max}/2\mu_{th})$  and  $\beta \approx \mu_{th}^2 \mu_{max}$  we have

$$cA \approx \frac{10}{\sqrt{N}} \frac{\mu_{max}}{\mu_{th} \ln(\pi\mu_{max}/2\mu_{th})}. \quad (10)$$

With typical for gravitationally lensed arcs values of  $\mu_{th} \sim 10$ ,  $\mu_{max} \sim 100$  (Lewis et al. 2000) and  $N \sim 10^4 - 10^6$  in a pixel  $cA \lesssim 0.01 - 0.1$ . This means that when talking about a deviation of at least one standard value  $\sigma$ , for which the Gaussian probability is  $\approx 0.15$ , one can be sure that the actual probability of such a deviation is not less than (5–25) per cent.

Strictly speaking, the minimum magnification value for microlensing at high optical depth is greater than one used in (i) as was shown by Schneider (1984), and

<sup>2</sup> The work of Jahreiss & Wielen (1997) presents V-band luminosities which are of rather limited interest for exact cosmological predictions where K-corrections are to be taken into account; however, these numbers provide sensible estimates for the quantities under consideration.

one could rather use some model value for this quantity (Bartelman & Schneider 1990). However, this does not have much impact on the estimate of the validity of our approximation. Perhaps more important is that due to the value of minimum magnification which is greater than unity, Gaussian approximation clearly cannot hold exactly as it assigns non-zero probability to flux values below the minimum. However, this inconsistency is well inside the uncertainty of our method, given by (10) and does not affect our results.

The initial task is thus reduced to calculating the only parameter of a centered Gaussian distribution – its dispersion. As  $\{L_i\}$  is not known *a priori* (and neither it can be known well *a posteriori*),  $\delta L|_{\{L_i\}}$  is to be averaged over all possible  $\{L_i\}$ . This can easily be done by considering the following three random variables:

$$\Delta L = \Delta L^o + \delta L \quad (11)$$

where  $\Delta L = \sum_i (\mu L_i - \bar{\mu} \langle L_i \rangle)$ ,  $\Delta L^o = \bar{\mu} \sum_i (L_i - \langle L_i \rangle)$  and  $\delta L$  is the value of interest. Here, again the bar denotes averaging in the  $\mu$  domain while angled brackets mean averaging over  $\{L_i\}$ .

As these three quantities are (nearly) Gaussian and uncorrelated (the correlation vanishes when averaging over  $\mu$ ), the following relation holds:

$$\sigma_{\delta L}^2 = \sigma_{\Delta L}^2 - \sigma_{\Delta L^o}^2. \quad (12)$$

Clearly,

$$\sigma_{\Delta L^o}^2 = \left\langle \left( \bar{\mu} \sum_i (L_i - \langle L_i \rangle) \right)^2 \right\rangle = N \bar{\mu}^2 \sigma_L^2 \quad (13)$$

where  $\sigma_L^2$  is the dispersion of individual flux (Jahreiss & Wielen 1997).

For the second quantity we may write:

$$\begin{aligned} \sigma_{\Delta L}^2 &= \overline{\left\langle \left( \sum_i (\mu L_i - \bar{\mu} \langle L_i \rangle) \right)^2 \right\rangle} \\ &= N \overline{\left\langle \mu^2 L_i^2 - 2\bar{\mu} \mu L_i \langle L_i \rangle + \bar{\mu}^2 \langle L_i \rangle^2 \right\rangle} \\ &= N (\bar{\mu}^2 \langle L_i^2 \rangle - \bar{\mu}^2 \langle L_i \rangle^2) \\ &= N (\sigma_\mu^2 \langle L_i^2 \rangle + \bar{\mu}^2 \sigma_L^2) \end{aligned} \quad (14)$$

and therefore

$$\sigma_{\delta L}^2 = N \langle L_i^2 \rangle \sigma_\mu^2. \quad (15)$$

The dispersion of the quantity  $\delta L / (N \bar{\mu} \langle L_i \rangle)$  – the relative fluctuation – is thus given by:

$$\epsilon_{\delta L}^2 = \frac{1}{N} \frac{\langle L_i^2 \rangle}{\langle L_i \rangle^2} \frac{\sigma_\mu^2}{\bar{\mu}^2}. \quad (16)$$

As  $N$  is not known either we will just divide the observed flux of the pixel  $L_{obs}$  by the mean magnification factor and mean individual stellar flux to get a first-order estimate:

$$\hat{N} = \frac{L_{obs}}{\bar{\mu} \langle L_i \rangle}. \quad (17)$$

Thus,

$$\hat{\epsilon}_{\delta L} = \sqrt{\frac{\langle L_i^2 \rangle}{\langle L_i \rangle L_{obs}}} \sqrt{\varepsilon_\mu^2 \bar{\mu}}, \quad (18)$$

with the first factor in this formula being approximately  $6.02/\sqrt{L_{obs}/L_\odot}$  for the luminosity function of Jahreiss & Wielen (1997) and the variability extent

$$\varepsilon_\mu^2 \equiv \frac{\sigma_\mu^2}{\mu^2} = \frac{\overline{\mu^2}}{\mu^2} - 1. \quad (19)$$

This quantity is therefore of our prime interest.

## 2.2 Evaluation of $\varepsilon_\mu^2$

In calculating the variability extent  $\varepsilon_\mu^2$  we employ the method of Neindorf (2003), who improved and generalized previous works of Deguchi & Watson (1987), Seitz & Schneider (1994) and Seitz, Wambsganss & Schneider (1994) to make possible the calculation of microlensing correlation functions in the case of non-zero shear. We, however, slightly modify his equations and evaluation method for our specific needs.

Let  $\mathbf{z}$  and  $\zeta$  be the light ray positions in the lens  $\mathcal{L}$  and source  $\mathcal{S}$  planes, respectively. The normalized lens equation is then (Kayser, Refsdal, Stabell 1986; Paczyński 1986)

$$\zeta = \hat{J}_o \mathbf{z} - \text{sign}(1 - \kappa_c) \sum_i m_i \frac{\mathbf{z} - \mathbf{z}_i}{|\mathbf{z} - \mathbf{z}_i|^2} \quad (20)$$

where

$$\hat{J}_o \equiv \begin{pmatrix} 1 + \gamma & 0 \\ 0 & 1 - \gamma \end{pmatrix} \quad (21)$$

Here  $\gamma = \gamma'/(1 - \kappa_c)$ , while  $\kappa_c$  is the smooth matter convergence and  $\gamma'$  is the shear, both expressed in critical units

$$\Sigma_o \equiv \frac{c^2}{4\pi G D} \quad (22)$$

and

$$\Gamma_o \equiv \frac{c^2}{4GD}, \quad (23)$$

where  $D$  is a reduced (angular diameter) distance

$$D \equiv \frac{D_{LS} D_{OL}}{D_{OS}}. \quad (24)$$

The masses of the microlenses  $m_i$  are given in units of  $M_o$  – the quantity which also defines Einstein radii  $z_o$  and  $\zeta_o$  – physical length units in which  $\mathbf{z}$  and  $\zeta$  of (20) are expressed – in lens and source planes:

$$z_o \equiv \sqrt{\frac{4GM_o}{c^2} \frac{1}{|1 - \kappa_c|} \frac{D_{LS} D_{OL}}{D_{OS}}} \quad (25)$$

$$\zeta_o \equiv \sqrt{\frac{4GM_o}{c^2} |1 - \kappa_c|} \frac{D_{LS} D_{OS}}{D_{OL}}. \quad (26)$$

In the case we consider the microlensing shear  $\mathbf{S}(\mathbf{z}) \equiv \text{sign}(1 - \kappa_c) \sum m_i (\mathbf{z} - \mathbf{z}_i) / |\mathbf{z} - \mathbf{z}_i|^2$  – the second term in (20) – is an isotropic random variable. Changing the sign of  $\gamma$  has the effect of only redefining coordinate axes and since this is not of interest for us we drop the  $\text{sign}(1 - \kappa_c)$  factor in (20) and use absolute value of  $\gamma$  from now on.

The magnification factor at a point  $\zeta$  in the source plane may be written in an elegant form (Neindorf 2003):

$$\mu(\zeta) = \frac{1}{|1 - \kappa_c|^2} \int_{\mathcal{L}} \delta(\zeta - \hat{J}_o \mathbf{z} + \mathbf{S}(\mathbf{z})) d^2 \mathbf{z}. \quad (27)$$

The average of  $\mu$  is

$$\mu_{th} = \frac{1}{|[1 - \kappa_c]^2[(1 - \kappa)^2 - \gamma^2]|} \quad (28)$$

where  $\kappa = \pi \langle m \rangle n$  is the scaled microlensing optical depth with  $n$  being the surface number density of microlenses and angled brackets now meaning averaging over microlens mass distribution  $\phi(m)$ .

We consider a Lambert disc – a disc of uniform surface brightness – with radius  $R$  in  $\zeta_o$  units and total flux  $I_o$ . The average value of *observed* flux  $\langle I \rangle$  does not depend on the microlens mass distribution and is only a function of lensing macro parameters:

$$\langle I \rangle = I_o \mu_{th} = \frac{I_o}{|(1 - \kappa_c)^2 \det \hat{J}|}$$

with

$$\hat{J} \equiv \hat{J}_o - \kappa \hat{1} = \begin{pmatrix} 1 - \kappa + \gamma & 0 \\ 0 & 1 - \kappa - \gamma \end{pmatrix}. \quad (29)$$

As shown in the Appendix A, the following relation holds for  $\varepsilon_\mu^2$ :

$$\varepsilon_\mu^2 + 1 = \frac{\langle I^2 \rangle}{\langle I \rangle^2} = \frac{2 |\det \hat{J}|}{\pi R^2} \int \int \int ds' dr d\chi \frac{1}{s'} \times \quad (30)$$

$$J_1^2 \left( R \frac{rs'}{2} \right) J_0 \left( \gamma \frac{r^2 s'}{2} \right) e^{-[na(s', \chi) + is' \cos \chi] r^2/2}.$$

The integration is done from zero to infinity in  $\rho$  and  $s'$  and from zero to  $2\pi$  in angular variable  $\chi$ . Function  $a(s, \chi)$  in this formula is given by Neindorf (2003) and is described in the Appendix A.

Introducing the function

$$B(s, \chi) \equiv \frac{na(s, \chi) + is \cos \chi}{s} = \quad (31)$$

$$\frac{\kappa}{\pi \langle m \rangle} \frac{a(s, \chi)}{s} + i \cos \chi$$

and performing the variable change  $r \rightarrow \rho = r^2 s/2$ ,  $s' \rightarrow s = R^2 s'/2$  we get the following integral to be evaluated:

$$\varepsilon_\mu^2 + 1 = \frac{|\det \hat{J}|}{\pi} \int_0^\infty ds s^{-2} \times \quad (32)$$

$$\int_0^\infty d\rho J_1^2(\sqrt{\rho s}) J_0(\gamma \rho) \int_0^{2\pi} d\chi e^{-\rho B\left(\frac{2s}{R^2}, \chi\right)}$$

This evaluation is done in Appendix B under the assumptions that  $R \leq 10^{-2} - 10^{-3} \ll 1$  and  $R \ll \gamma$ .

The former is plausible, since in a cosmological situation with  $D \sim 10^{28}$  cm, the length scale (26) is

$$\zeta_o \sim 10^{17} \left( \frac{M_o}{M_\odot} \right)^{1/2} |1 - \kappa_c|^{1/2} \text{ cm},$$

while typical physical sizes of sources are  $\sim 10^{10} - 10^{12}$  cm. However, it immediately places a constraint on the microlens masses and the smooth component convergence:

$$M_o |1 - \kappa_c| \geq 10^{-4} M_\odot. \quad (33)$$

Therefore the results derived below are not directly applicable to situations where (33) is not fulfilled, which may be of interest when Jupiter-mass lenses are involved or for detailed investigations of microlensing in the region  $|\kappa_c - 1| \ll 1$ . Microlensing of large sources was considered numerically by

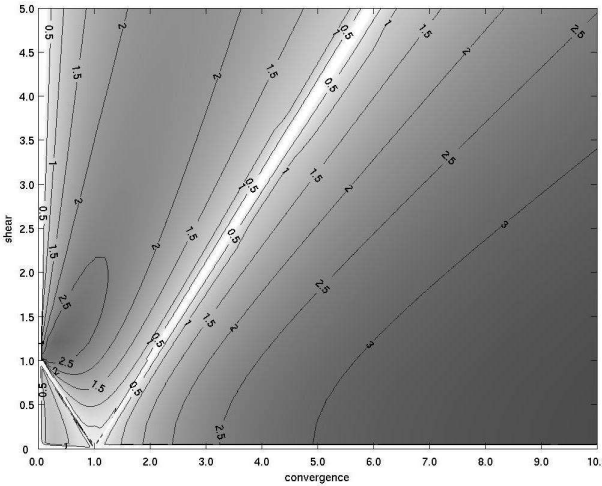


**Figure 1.** The contour lines of  $\varepsilon_\mu$  as a function of convergence in microlenses  $\kappa$  and shear  $\gamma$ .

Refsdal & Stabell (1991) in the zero shear case and later including the effect of a shear term (Refsdal & Stabell 1997). Quite naturally, increasing the size of the source suppresses microlensing-induced fluctuations, averaging them over less correlated regions of the magnification map. However, for sources as large as  $R \sim 30$  they find values of  $\varepsilon_\mu \sim 0.1$  in a range of  $0 \leq \kappa \leq 2$  and  $0 \leq \gamma \leq 0.4$  (it was found that  $\varepsilon_\mu^2 \approx 2\kappa/R^2$  in zero shear case). This is only an order of magnitude less than the numbers we obtain below and shows, that even objects billions times less massive than the Sun could introduce noticeable variability provided they contribute to the overall compact object density (however, the time scale of this kind of variability will be much shorter).

The second assumption – which relates  $\gamma$  and  $R$  – is of a rather technical nature and does not restrict our scope whenever marginal cases of zero shear are not considered.

As shown in the Appendix B, under these assumptions the integral (32) may be then rewritten in the following form:

$$\varepsilon_\mu^2(\kappa, \gamma, R) = \frac{|\det \tilde{J}|}{\pi} \left[ I(\kappa, \gamma) - \frac{g_3(\kappa, \gamma)}{2} \ln R \right] - 1, \quad (34)$$

where  $I(\kappa, \gamma)$  and  $g_3(\kappa, \gamma)$ , defined by (B22) and (B13), are computed numerically. The actual values of  $g_3(\kappa, \gamma)$  do not exceed  $\sim 0.1 - 0.2$ . Therefore we neglect the weak dependence of  $\varepsilon_\mu^2$  on  $R$  putting  $R_o = 10^{-6}$ .

The contour lines of constant  $\varepsilon_\mu$  are shown in Figure 1 for the range of parameters  $\kappa$  and  $\gamma$  present in the observed clusters. Computations near the lines  $\gamma = |1 - \kappa|$  are unreliable and are therefore ignored on the graph.

### 2.3 Dependence on source redshift and smooth matter contribution

The actual values of  $\kappa$  and  $\gamma$  depend on both the physical surface density at the point in the lensing plane where the image is formed and the scaling parameters  $\Sigma_o$  and  $\Gamma_o$  given by (22,23) which in turn are functions of the distance parameter  $D$  (24) and thus – of lens and source redshifts and underlying cosmology. If we consider the redshift of the lens  $z_l$  as fixed, the values of convergence and shear would de-

pend on the source redshift  $z_s$ . As  $\Sigma_o \propto D^{-1}$  and  $\kappa \propto \Sigma_o^{-1}$  and the same applies to the shear,  $\kappa$  and  $\gamma$  are directly proportional to  $D$  and can be written in a simple form:

$$\begin{pmatrix} \kappa \\ \gamma \end{pmatrix} = \begin{pmatrix} \kappa_o \\ \gamma_o \end{pmatrix} \frac{D(z_s)}{D(z_s^o)}. \quad (35)$$

with  $\kappa_o$  and  $\gamma_o$  being the convergence and shear corresponding to a given redshift  $z_s^o$ .

For the currently favoured flat cosmological models ( $\Lambda = 1 - \Omega_o$ )

$$D(z_s) \propto \frac{f(z_s) - f(z_l)}{f(z_s)} = 1 - \frac{f(z_l)}{f(z_s)},$$

where

$$f(z) = \int_0^z \frac{d\zeta}{\sqrt{\Omega_o(\zeta + 1)^3 + 1 - \Omega_o}}. \quad (36)$$

As  $f(z)$  is a monotonic increasing function of its argument and  $z_s$  is clearly greater than  $z_l$ , the second fraction in (35)

$$h(z_s, z_s^o) \equiv \frac{D(z_s)}{D(z_s^o)} = \frac{1 - f(z_l)/f(z_s)}{1 - f(z_l)/f(z_s^o)} \quad (37)$$

increases from zero at  $z_s = z_l$  through unity at  $z_s = z_s^o$  to some limiting value  $h_\infty$  – determined by  $z_l$ ,  $z_s^o$  and  $\Omega_o$  – when  $z_s \rightarrow \infty$ . This is somewhat different from considering convergence and shear as functions of  $z_l$ , in which case there exists an optimal lens redshift which maximizes the lensing parameters. In the case of varying  $z_s$  the further the source is the greater  $\kappa$  and  $\gamma$  are. For instance, in the case of Abell 370 with  $z_l = 0.37$ ,  $h_\infty \approx 1.7$  for  $\Omega_o = 1$  and about 1.5 when  $\Omega_o$  is only 0.2 ( $z_s^o = 1$ ) – that is,  $\kappa$  and  $\gamma$  for far away sources are not much larger than for sources at redshifts of about unity.

The behaviour of  $\varepsilon_\mu$  with redshift is evidently more complex – as  $\kappa$  and  $\gamma$  slide along the line of proportionality (35) in  $\kappa$ – $\gamma$  plane the variance first increases from zero at its bottom left corner but can then, depending on  $\kappa_o$  and  $\gamma_o$  cross one or two ‘zero-signal’ lines  $\gamma = |1 - \kappa|$ . Actual  $z_s = 1$  convergence and shear in Abell 370 and Abell 2218 for which we have detailed density maps (Bézecourt et al. 1999; Kneib et al. 1996) cover approximately the range present on figure 1 therefore there is no much point in discussing how  $\varepsilon_\mu$  changes with redshift any further, specially since the measurements of the redshift have been performed for many of the potential targets for surface brightness variability observations.

However, it is worth noting the general pattern of brightness variability behaviour over the area of some of the most prominent candidates for this sort of observations – gravitational lensed arcs. These objects often consist of two or more sections with critical lines between these sections and, in the case where there is no smooth matter, the variability will be most easily observed in the pixels further away from the critical lines on which  $\det \tilde{J}$  – and variability – vanish.

When compact objects make up only a limited fraction of the lensing matter – which is expected to be the case – the situation is more interesting. Let  $x$  be the compact objects share in the total convergence, so that  $\kappa' = x\kappa_{tot}$  and  $\kappa_c = (1 - x)\kappa_{tot}$ . Then the effective convergence and shear are  $\kappa = x\kappa_{tot}/|1 - (1 - x)\kappa_{tot}|$  and  $\gamma = \gamma'/|1 - (1 - x)\kappa_{tot}|$ .

The factor  $\det \hat{J}$  in  $\epsilon_\mu^2$  is then:

$$\det \hat{J} = (1 - \kappa)^2 - \gamma^2 = \frac{[(1 - (1 - x)\kappa_{tot})^2 - x\kappa_{tot}]^2 - \gamma'^2}{[1 - (1 - x)\kappa_{tot}]^2} = \frac{1}{[1 - (1 - x)\kappa_{tot}]^2} \left\{ \frac{[(1 - \kappa_{tot})^2 - \gamma'^2]}{[(1 - (1 - 2x)\kappa_{tot})^2 - \gamma'^2]} \right\} \quad (38)$$

the latter alternative determined by whether  $\kappa_{tot}$  is less (top) or greater (bottom) than  $(1 - x)^{-1} \geq 1$ .

Therefore, the outer lines of the zero variability signal (those which correspond to  $\gamma = 1 - \kappa$  and therefore  $\kappa < 1$ ) are not affected by the addition of smooth matter. Other zero line positions depend on the value of  $x$  and this dependence represents a potential means to determine this value. We will see that only highly magnified pixels show variability detectable with present-day observational techniques – i.e., those lying near the critical curves, and therefore for the effect to be detectable these curves should not coincide with the lines of zero variability. Thus, the condition  $\kappa_{tot} \geq (1 - x)^{-1}$  or, since  $\kappa_{tot}$  can be determined from macrolensing modeling:

$$x \leq 1 - 1/\kappa_{tot} \quad (39)$$

is in practice necessary to observe the effect. For axially symmetric clusters, the arcs which form on the second (inner) critical curves tend to have radial morphology, i.e. their dimensions along the critical curve – and thus the number of highly magnified pixels – are small.

As an example we have computed the maps of the signal  $\epsilon_\mu$  for two well-studied clusters - Abell 370 and Abell 2218 (see Kneib et al. 1996; Bézecourt et al. 1999; Metcalfe et al. 2003 and references therein) and present them in figures 2 and 3. These are given for two values of the source redshift  $z_s = 2$  for both clusters and  $z_s = 0.724$  and  $z_s = 0.702$  for Abell 370 and Abell 2218, respectively. The latter two correspond to giant gravitational-lensed arcs seen in the clusters while the former are given for comparison. As new instruments – like *James Webb Space Telescope* (JWST, formerly known as NGST) – come into operation they are expected to observe many more lensed galaxies behind these clusters and  $z_s = 2$  maps show how the signal might look for them. Each of the maps is given for two values of  $x$  with 100 and 20 per cent of convergence contained in compact objects. These values of  $x$  are assumed to be constant over the maps.

In Figure 4 we show the contour lines of the microlensing signature  $\epsilon_\mu$  superimposed on the optical image of the radial arc R in Abell 370 obtained with the *Hubble Space Telescope* (HST) (Bézecourt et al. 1999). The source redshift here is estimated to be  $z_s \approx 1.7$  (see Bézecourt et al. 1999 and Smail et al. 1996). The regions between the thick white lines correspond to ‘zero signal’ lines where  $\epsilon_\mu \leq 0.3$ , while the regions between the thick black lines – where present – have  $|\kappa_c - 1| \ll 1$ , where the analysis given in this paper is not applicable. Dashed white lines show the location of the critical curve.

The figure illustrates how the signal changes with varying fraction of compact objects in the overall mass budget. Perhaps in contrast to naive expectations, the signal generally increases when the density of compact objects is decreased because of the magnification effect by the smooth matter distribution. This can be understood on the basis of (34): the dependence of the variability extent on the

source size is rather modest while slight changes in the smooth matter convergence  $\kappa_c$  change the  $|1 - \kappa_c|^{-1}$  factor in the definition of effective shear and convergence of the compact matter (Kayser et al. 1986; Paczyński 1986) significantly when  $\kappa_c$  is about unity which is a common place for macrolensed images of distant sources; thus convergence and shear on the  $\kappa - \gamma$  plane of Fig.1 can assume high values. This somewhat surprising behaviour has also been discussed by Schechter et al. (2003) while Schechter & Wambsganss (2002) give a detailed explanation of this effect. More important is the change in zero signal lines pattern that can be readily probed in observations and can provide, via (38), an interesting constraint on the compact object contribution to the overall convergence determined by modeling of the lensing potential.

For images which do not lie on the critical lines observations can still be of interest for the determination of  $x$  through studying the variability pattern in greater detail and comparing it to the predicted one. However, for the two clusters investigated in this paper the latter possibility remains mostly a theoretical one because of observational limitations.

### 3 OBSERVATIONAL ASPECTS

Let us now discuss the prospects for the detection of the considered effect. We will consider observations with *Hubble Space Telescope* as a reference point in this section although it will be clear that observations of this effect with HST in the two clusters under investigation is impractical. Observations with more advanced instruments, such as *James Webb Space Telescope* or the proposed 30-metre telescope (also known as CELT)<sup>3</sup> could, however, be used to observe the microlensing-induced variability.

The number of photons  $l$  detected in a unit time interval in a pixel from a source of observed luminosity  $L_{obs}$  (uncorrected for lensing magnification) is determined by the luminosity distance to the source  $D_L(z_s)$ , the energy distribution in its spectrum  $f_\lambda$  (such that  $\int d\lambda f_\lambda = 1$ ) and the telescope efficiency  $\eta_\lambda$  and diameter  $d$ :

$$l = \frac{d^2 L_{obs}}{16D_L^2(z_s)} \int d\lambda f_\lambda ((1 + z_s)^{-1} \lambda) \eta_\lambda(\lambda) \frac{\lambda}{hc} = L_{obs} d^2 \eta_{eff} \lambda_{eff} / 16D_L^2(z_s) hc = \alpha L_{obs} \quad (40)$$

These photons will be accompanied by  $b$  background photons. For HST Wide Field and Planetary Camera 2 (WFPC2) and actual luminosities observed in pixels of gravitationally lensed galaxies, the noise is dominated by Poissonian fluctuations in count numbers. At  $z_s = 1.7$  the coefficient in (40) is  $\alpha \approx 5 \cdot 10^{-6} L_\odot^{-1} \cdot \text{hour}^{-1}$  while the background level is about  $b = 1000$  photons in a pixel per hour (this value changes by about 1.5–2 depending on the source heliocentric ecliptic longitude).

Let us now calculate the time  $t$  required to detect the fractional change of  $\beta \epsilon_{\delta L}$  in a pixel with given microlensing parameters  $\epsilon_\mu, \bar{\mu}$  at a signal-to-noise level  $Q$ ;  $\beta$  here determines the fraction of pixels deviating from the mean at  $\beta \epsilon_{\delta L}$  level via the normal law  $1 - \Phi(\beta)$  and we will use  $\beta = 1$  for

<sup>3</sup> See <http://tmt.ucolick.org/> for details

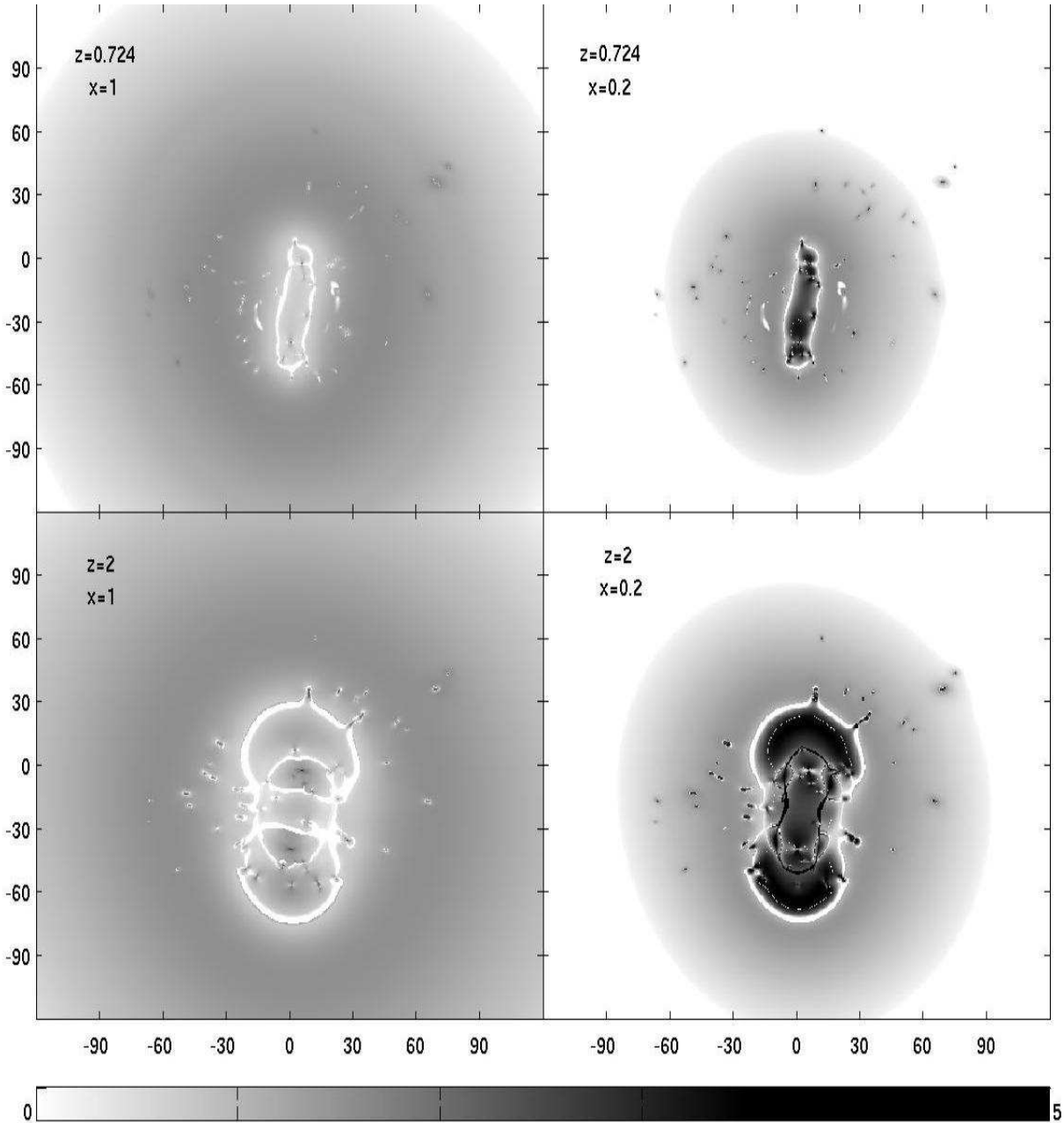


**Figure 2.** The map of microlensing-induced variability parameter  $\varepsilon_\mu$  over the area of the cluster Abell 370. Coordinates are given in arc seconds, orientation of the images as the same as in Bézecourt et al. (1999) - the north is to the top, the east is to the left. The maps are given for two redshift values  $z = 0.724$  and  $z = 2$  and for two values of compact object mass fraction  $x = 1$  and  $x = 0.2$  (for  $x = 1$  white lines of  $\varepsilon_\mu$  coincide with the macrolensing critical lines, according to (38)). The thick black lines at  $x = 0.2$  correspond to regions with  $|\kappa_c - 1| \ll 1$  where the analysis given in this paper is not applicable.

numerical estimates which is close to the optimal value. The signal  $S$  is

$$S = \beta \varepsilon_{\delta L} l t \quad (41)$$

while the noise  $N$  is determined by Poissonian fluctuations

$$N = \sqrt{2bt + (2 + \beta \varepsilon_{\delta L})lt}, \quad (42)$$

the factor of 2 in the latter expression comes from the fact that we need to compare two images from different epochs. In most cases  $\varepsilon_{\delta L}$  can be neglected for noise estimation. Equation (16) shows that signal and noise behave similarly

which, as can be easily seen, gives the following expression for the time required:

$$t = Q^2 \frac{2\langle L_i \rangle}{\langle L_i^2 \rangle \alpha} \frac{1 + b/l}{\beta^2 \varepsilon_\mu^2 \bar{\mu}}. \quad (43)$$

Thus, it is determined mostly by the telescope and geometry (through  $\alpha$ ) and lensing characteristics of the pixel (through  $\varepsilon_\mu$  and  $\bar{\mu}$ ) while the dependence on photometry is very weak as soon as the background value is exceeded by the source surface brightness and increases inversely proportional to the latter if it is lower than the sky level. In fact, the surface

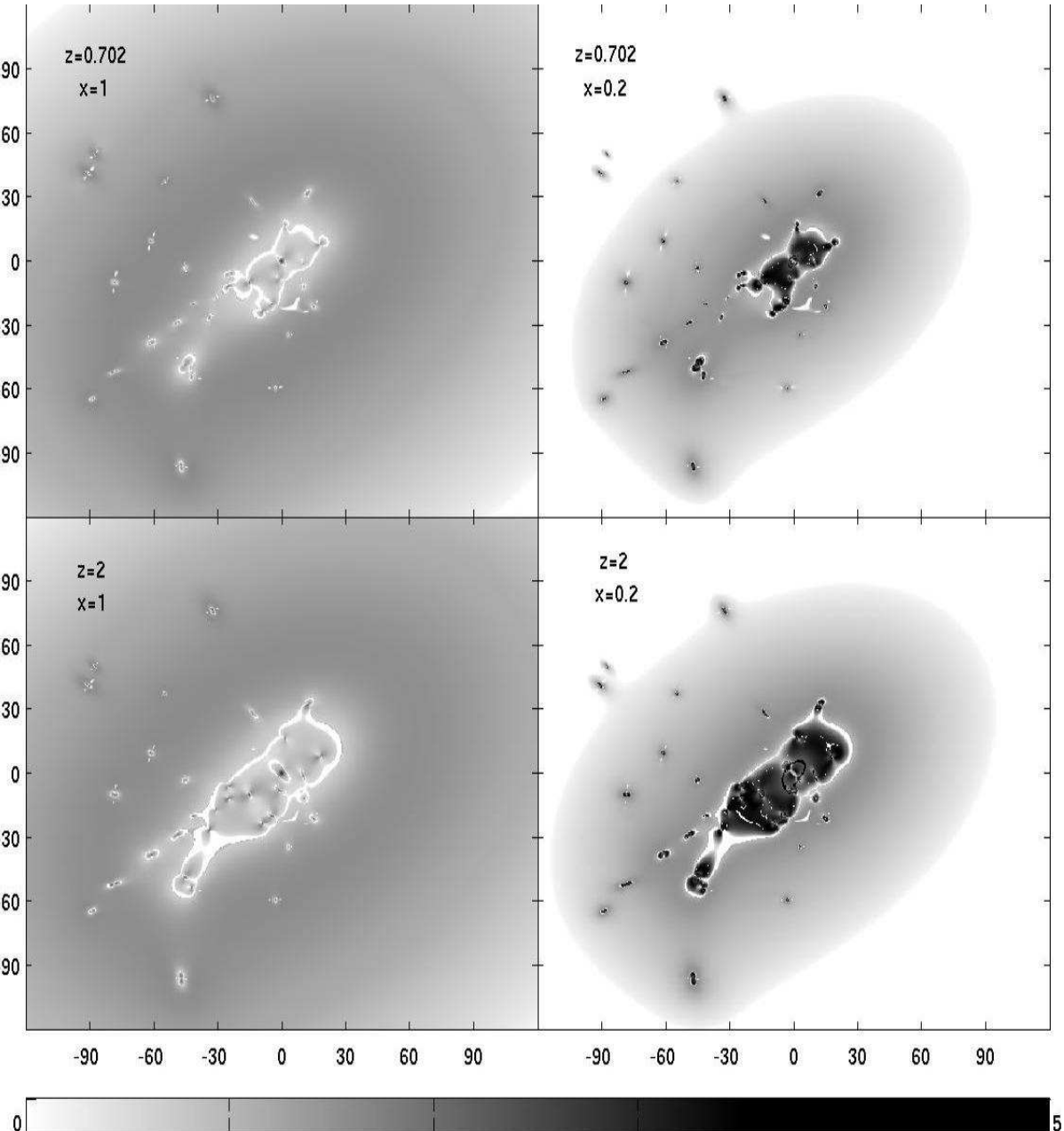


**Figure 3.** The map of microlensing-induced variability parameter  $\varepsilon_\mu$  over the area of the cluster Abell 2218. Orientation is the same as in figure 2. The maps are given for two redshift values  $z = 0.702$  and  $z = 2$  and for two values of compact object mass fraction  $x = 1$  and  $x = 0.2$  (for  $x = 1$  white lines of  $\varepsilon_\mu$  coincide with the macrolensing critical lines, according to (38)). The thick black lines at  $x = 0.2$  correspond to regions with  $|\kappa_c - 1| \ll 1$  where the analysis given in this paper is not applicable.

brightness of a typical galaxy at  $z = 0$  is of order  $21^m - 22^m$  per sq.arcsec and scales as  $(1 + z)^{-(4-p)}$  with  $p$  depending on the spectrum; surface brightness is conserved in gravitational lensing. The sky background outside the Earth's atmosphere varies in the range of  $22^m - 23^m$  per sq.arcsec and is about half a magnitude higher for the best terrestrial observatories. Therefore, typical values of the numerator in the last fraction of (43) is of order 1 for nearby galaxies and grows rapidly as the redshift exceeds unity.

Combining values of coefficients in (16) and (40) we find that for observation of the radial arc in Abell 370 with HST WFPC2 the value of the first fraction in (43) is ap-

proximately  $1.2 \times 10^4$  hours. The value of the variability power parameter  $\varepsilon_\mu^2$  does not exceed  $\sim 15 - 20$  (in fact,  $\varepsilon_\mu^2$  changes very slowly with convergence after it exceeds approximately 15) while the ratio of sky background to the observed arc surface brightness  $b/l$  for most pixels is about 7 – 8 (Bézecourt et al. 1999).

Therefore the effect can be most easily observed in pixels of high magnification  $\bar{\mu}$ . This value does not depend on the compact-to-smooth convergence ratio, and peaks at the critical curve. The variability  $\varepsilon_\mu^2$ , on the contrary, follows the compact matter distribution and wherever some smooth matter is present, can preserve high values at the regions of

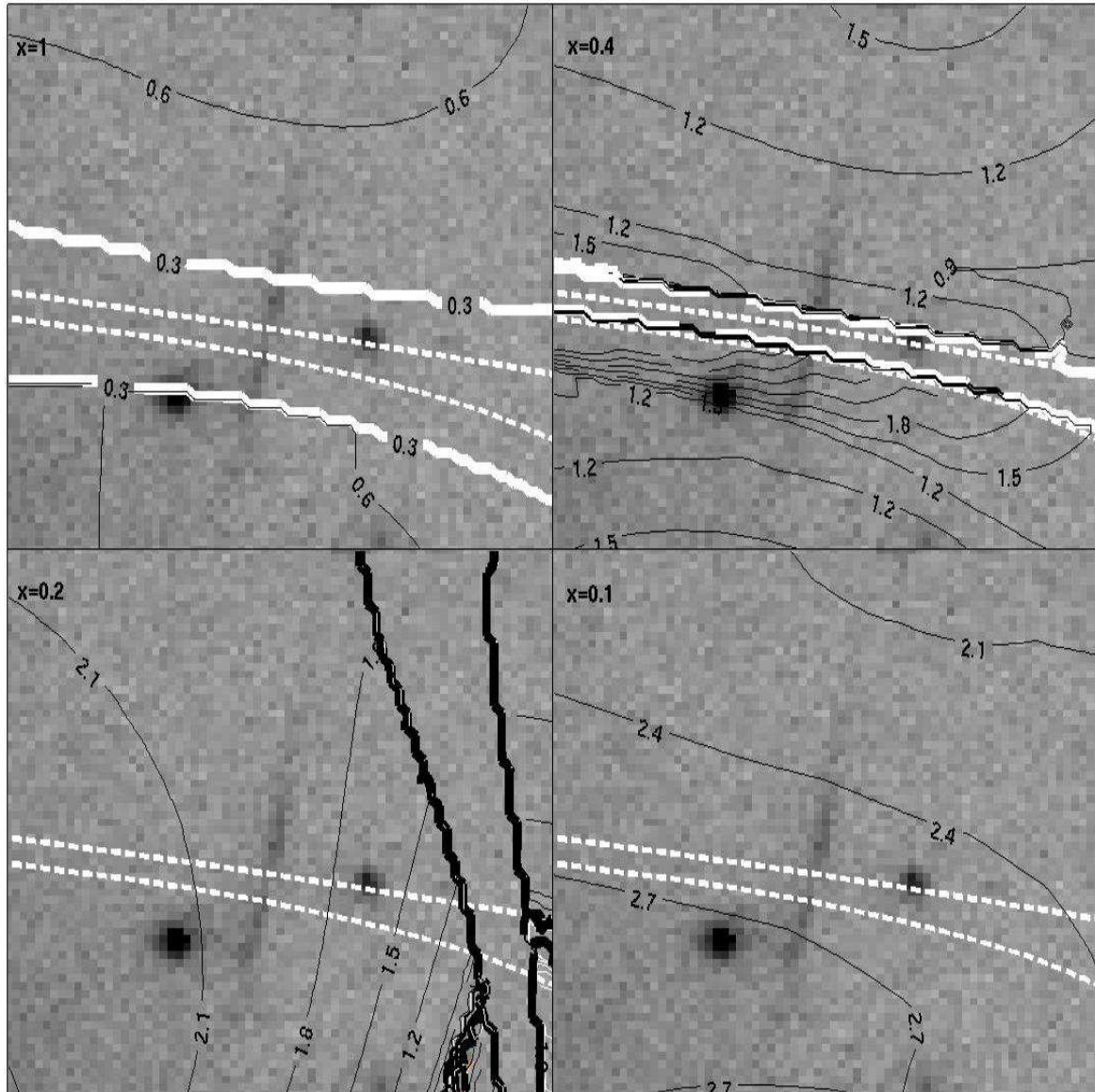


**Figure 4.** The contour lines of microlensing-induced variability parameter  $\varepsilon_\mu$  superimposed on the optical image of the radial gravitationally lensed arc ( $z \approx 1.7$ ) seen in Abell 370 obtained with the *Hubble Space Telescope* (Bézecourt et al. 1999). The area between the solid white lines correspond to nearly zero signal with  $\varepsilon_\mu \leq 0.3$ . The dashed white lines represent the approximate location of the critical curve, while the area between the thick black lines correspond to  $|\kappa_c - 1| \ll 1$  where the analysis given in this paper is not applicable. Four values of compact to total mass density ratio are assumed:  $x = 1.0$ ,  $x = 0.4$ ,  $x = 0.2$  and  $x = 0.1$ .

high magnification. As can be seen from (38) this is the case when the local convergence value is greater than the inverse of the smooth matter share  $(1 - x)^{-1}$ , or  $x \leq 1 - 1/\kappa_{tot}$ ; otherwise the variability zero lines coincide with the critical curves and it is not possible to get both appreciable variability and high magnification values. Somewhat ironically, the compact objects can only be observed when their mass contribution is sufficiently low.

Magnification values are determined firmly by the present-day advanced methods of mass distribution modeling in lensing clusters which proved to be accurate as

well as highly and successfully predictive (Kneib et al. 1993; Ebbels et al. 1998). The values of convergence for the radial arc R in Abell 370 span a range of approximately 1.3 to 1.4 and therefore the maximum values of the fraction of compact matter which produce detectable signal would be approximately 23 to 30 per cent – values close to those suggested by studies of the Galaxy and its immediate neighbourhood (Alcock et al. 2000; Lasserre et al. 2000; Sadoulet 1999). All other gravitationally lensed objects in the cluster either lie on the outer critical curves (e.g., the giant gravitationally

lensed arc A0) or do not show sufficient magnification values.

For the map of variability present on Figure 4 with  $x = 0.2$ , the values of  $\varepsilon_\mu^2$  on the arc are about four while the magnification varies from a few dozen to a few hundreds with a handful of pixels where  $\bar{\mu}$  exceeds  $10^4$ . Therefore, according to eqn. (43), for most pixels detecting variability at signal-to-noise ratio  $Q = 5$  with HST would require considerable integration time of a few hundreds to a few thousands hours. However, for a few pixels these exposure times will have more reasonable values of order ten hours.

Certain reservations should be made reflecting the fact that these values are dependent on the model and in this respect the distribution of the magnifications (or the derived required exposure times) is a more robust measure. However, one should keep in mind that the critical curve is necessarily a set of points with infinite magnification and therefore the number of variable pixels is determined by the length of the arc along the critical curve (which is rather small for radial arcs) and the rate at which magnification falls off the critical curve – i.e., graduality in convergence and shear values over the image in the critical curve vicinity.

To estimate the latter value, we can rewrite (43):

$$t = t_o \times \frac{1}{\bar{\mu}}, \quad (44)$$

where

$$t_o \equiv Q^2 \frac{2\langle L_i \rangle}{\langle L_i^2 \rangle \alpha} \frac{1+b/l}{\beta^2 \varepsilon_\mu^2}, \quad (45)$$

which is about  $6 \times 10^5$  hours for the radial arc R observed with HST. Factor  $1/\bar{\mu}$  vanishes at the critical curve, and to the first order approximation,  $t$  as a function of the coordinate  $d$  orthogonal to the critical curve is

$$t = t_o |\nabla \frac{1}{\bar{\mu}}| d. \quad (46)$$

Hence, the width of the strip along the critical line on which the required integration time  $t$  is less than a given value  $T$  is simply

$$2d = \frac{2T}{t_o |\nabla \frac{1}{\bar{\mu}}|} \geq \frac{T}{t_o} \frac{1}{|1 - \kappa_{tot}| |\nabla \kappa_{tot}| + \gamma' |\nabla \gamma'|}. \quad (47)$$

For the patch of the critical curve near the radial arc with  $\varepsilon_\mu^2 \approx 4$ ,  $1+b/l \approx 7-8$ ,  $\kappa_{tot} - 1 = \gamma' \approx 0.3$ ,  $|\nabla \kappa_{tot}| \approx 2 \times 10^{-3} \text{ pix}^{-1}$ ,  $|\nabla \gamma| \approx 3 \times 10^{-3} \text{ pix}^{-1}$  and  $\beta = 1$  one gets  $2d \approx T/600^h$  for HST. Multiplied by the dimension of the arc along the critical curve (about five for the radial arc R in Abell 370), these give the required number of pixels.

It is immediately clear from this estimate that since integration time of more than 100 hours is hardly possible, only local (on inter-pixel scale) stationary points in  $1/\bar{\mu}$  can give detectable signal for HST images – the above mentioned strip itself is too narrow. One would need more advanced telescopes to observe the effect, such as JWST or CELT, – or explore other lensing clusters where strongly lensed objects on inner critical curves are seen.

At visible and near-infrared wavelengths, the sky background level expected to be observed with JWST is not much different from that with HST and therefore changes mostly come from differences in the optics and spectral band via the value of  $\alpha$  in eqn. (43). Using the JMS sensitivity

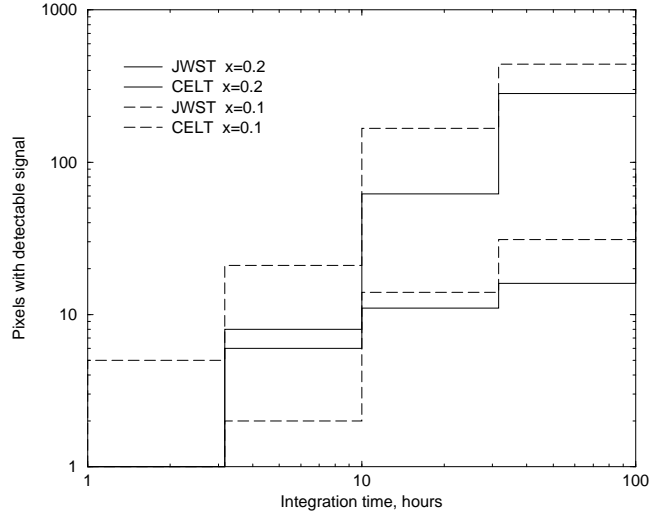


**Figure 5.** The number of pixels with detectable microlensing signature as a function of integration time required for the one  $\varepsilon_\mu$  variation to be detectable at five sigma level.

calculator<sup>4</sup> we estimate that the exposure time required for the *Near-InfraRed Camera* of JWST to detect the signal will be about 15 to 20 times as short as those of HST. However, even this would require exposure times of several dozen hours as  $2d \approx T/30^h$  in this case. In light of the recent discovery of a candidate  $z = 10$  lensed galaxy behind Abell 1835 (Pello et al. 2004), it does not seem implausible that such ultra-deep exposures with JWST will be attempted. For the radial arc in Abell 370 that would result in about a dozen variable pixels.

The proposed 30-metre telescope would make the prospects more optimistic. For a ground-based telescope, the sky background will be a factor of 1.5 – 2 higher, and the atmosphere transparency should be taken into account. However, increase in collecting area over the HST will be enormous, and the net effect will be to reduce  $t_o$  to about  $8 \times 10^3$  hours. Of further advantage would be the use of diffraction-limited mode. Taking into account possible tracking uncertainties, an estimate for the angular resolution of  $\sim 0.01$  arcsec should be considered conservative. This represents a five-fold decrease in the pixel size resulting in the ability to get closer to the critical curve. Thus, according to (47), the width of the strip around the critical curve where variability can be detected in  $T$  hours integration time would make  $2d \approx T/1^h$ . Similarly, the arc length along the critical curve will be covered by five times more pixels compared to HST. This means dozens of variable pixels and potential to observe the pattern of variability change both along and across the critical curve in just a few hours long exposure!

Figure 5 presents the histograms of the number of pixels in the image of the radial arc seen in Abell 370 which are expected to show variability detectable at the  $5\sigma$  level as a function of integration time for JWST and CELT. The actual values of the arc brightness are used to determine  $t$  from (43) for every pixel which are then binned logarithmically in 0.5 dex wide bins. Two values of the compact matter fraction  $x = 0.2$  and  $x = 0.1$  are assumed. For JWST, the

<sup>4</sup> See [http://www.stsci.edu/jwst/science/jms/jms\\_flux\\_form.html](http://www.stsci.edu/jwst/science/jms/jms_flux_form.html)

pixel size and background level are taken to be equal to those for HST WFPC2. For CELT, the background level is half a magnitude brighter while for the pixel size a value of 0.01 arcsec is assumed.

One should bear in mind that the pixels mentioned above are variable at a detectable level, but they will only spend about one-third of the time in this ‘varied’ state. This fraction of time can be controlled by the parameter  $\beta$  but one can see – combining (43), the normal distribution and the nearly linear histogram shape in the region of interest – that the value  $\beta = 1$  is close to optimal.

The time scale of variations depends on the microlens masses and motion and is of order months to years for Solar masses moving with a velocity of a few hundred kilometres per second (Lewis et al. 2000). Observation epochs should therefore be separated by a similar time interval.

#### 4 DISCUSSION

We have shown in the previous section that with a few exposures on JWST or CELT we expect to detect shimmering of pixels in the image of the radial gravitationally lensed arc in Abell 370 due to microlensing by compact objects in the cluster. To answer the question of how such detections should be interpreted let us now sketch a portrait of a typical event. This would also give us an insight into what sort of contaminants could mimic variability due to gravitational microlensing.

The surface brightness of the arc is about seven to eight times lower than the sky background level outside the Earth atmosphere. In a 30 hours-long exposure on JWST about 60 thousand ‘signal’ photons will be detected in a typical pixel and around 500 thousand background photons will accompany them. Hence the noise, according to (42), is approximately (neglecting  $\beta\varepsilon_{\delta L}$ ) 1060 photons and five times that is 5300 photons or about 9 percent of the original flux. As  $\varepsilon_\mu$  in this region is about 2 (see Fig. 4C), the pixel, according to (16) contains light of approximately  $4.7 \times 10^4$  stars with an intrinsic luminosity of some  $1.4 \times 10^4 L_\odot$ . Given a typical observed luminosity of  $2 \times 10^8 L_\odot$  the magnification needed is  $\sim 10^4$ , in accordance with the estimate of the previous section.

Nine per cent variability corresponds to  $0.09 \times 2 \times 10^8 / \bar{\mu} L_\odot = 1.8 \times 10^7 / \bar{\mu} L_\odot$  and the average value of magnification in the map is about a hundred. In the case of the average pixel, only supernova and brightest peak nova eruptions can give the true increase of  $\sim 10^5 L_\odot$ . The most significant contaminant to the average pixel is nova eruptions. We can calculate the expected number of nova explosions in a way similar to that of Baltz et al. (2003) – for a galaxy similar to the Milky Way the rate of nova explosions is expected to be  $10^{-9} - 10^{-10}$  eruptions per star per year. Eruption durations – by which we mean the period of time novae stay above the level of interest  $\sim 10^5$  – is only a fraction  $\sim 0.01 - 0.1$  of a year, long compared to the integration time while short compared to the interval between exposures. Therefore we expect about  $10^{-10}$  erupted novae per star at any given exposure. The radial arc spans around three hundred pixels and therefore the expected number of stars in it is about  $10^{10}$  – i.e., this is a galaxy of rather modest size. Thus, even not taking into account the multiple nature of the arc, novae

are not a problem for our study. Clearly, supernova explosions in the source galaxy are even less of a problem. An additional source of contamination is supernovae in background galaxies but, with a rate of  $10^{-3} - 10^{-2}$  SNe per galaxy between two exposures (see Sarajedini, Gilliland and Phillips 2000), they are not important.

However, with pixels magnified by a factor of  $\sim 10^4$  which is needed to observe the microlensing variability, physical luminosity changes go down to about two thousand Solar luminosities or less, and this is about the amplitude of the brightest Mira variables in red bands. Contamination due to Miras (as well as other variable stars) in microlensing studies is usually removed by considering observations in different spectral bands. The three key signatures of microlensing origin of the variability are achromaticity, uniqueness and a symmetric form of the variations (Paczyński 1986). None of them is valid in the case considered in this paper. Achromaticity does not work for pixel lensing although in the case of low optical depth some constraints can still be applied (Gould 1996). When the optical depth is high every star in the pixel at any given moment is subject to strong microlensing and this fact does not allow to use achromaticity constraint. For the same reason the uniqueness of the microlensing event does not work any more. With regards to the symmetry, we do not observe individual light curves in this case and therefore cannot use this constraint at all.

However, although we cannot use achromaticity for individual pairs of measurements, this property is still valid in a statistical sense. Namely, the variability extent seen in different bands is, according to (16), proportional to  $\langle L_i^2 \rangle / \langle L_i \rangle^2$  – the value which does not change much from one band to another, is closely related to the magnitude of the surface brightness fluctuations and can be determined in observations of nearby galaxies which are definitely not lensed. In contrast, (absolute) variability amplitude of variable stars is strongly dependent on the spectral band and, for instance, in Miras the change ranges from thousands Solar luminosities in K band to hundreds and even tens of Solar luminosities in bluer bands. Other variables are too faint to affect the fluxes of pixels containing thousands of stars.

Contamination due to variable stars is a more serious issue for observations with CELT. An analysis similar to the one given above, shows that typical intrinsic luminosities of pixels with variability detectable in a one hour long exposure amount to just around 500 solar luminosities with typical variability extent of around 70 per cent or around 350 solar luminosities. This is a range at which various variable stars may contribute to the observed variability. The only way to distinguish it from the variability due to gravitational microlensing by compact dark matter in the cluster seems to be to use the behaviour of variability from one pixel to another and across spectral bands to see whether it is consistent with physical variability or gravitational microlensing hypotheses.

One of the remaining problems is how to tell the difference between no compact matter and too much compact matter in the case of a null signal detection. More work needs to be done on this question and perhaps other effects should be considered to answer it. However, the effect considered provides us with a lot of information on the microlensing population. The Gaussian approximation seems to be a simple framework for characterizing pixel microlens-

ing in galaxy clusters and although the implications of future observations on microlensing population are not straightforward, they can provide strong constraints on the otherwise unaccessible properties of this population.

## ACKNOWLEDGMENTS

AVT is supported by IPRS and IPA from the University of Sydney and wishes to express his gratitude to Bernd Neindorf, Dmitry Klochkov and Mark Walker for useful discussions. GFL thanks OutKast for Hey Ya. JPK acknowledges support from Caltech and CNRS. Authors wish to thank Tim Bedding, Michael Scholz and Mike Ireland for useful explanations concerning Miras' variability and the referee for important observations.

## REFERENCES

Alcock C. et al., 2000, ApJ, 542, 281  
 Ansari R. et al., 1997, A&A, 324, 843  
 Baillon P., Bouquet A., Giraud-Héraud Y., Kaplan J., 1993, A&A, 277, 1  
 Baltz E.A., Lauer T.R., Zurek D.R., Gondolo P., Shara M.M., Silk J., Zepf S.E., astro-ph/0310845  
 Bartelman M., Schneider P., A&A, 1990, 239, 113  
 Berry A.C., 1941, Trans. Amer. Math. Soc., 49, 122  
 Bézecourt J., Kneib J.-P., Sousail G., Ebbels T.M.D., 1999, A&A, 347, 21  
 Chistyakov G.P., 2001, Theory Probab. Appl., 46, 2, 226  
 Crotts A.P.S., 1992, ApJ, 399, L43  
 Crotts A.P.S., Tomaney A.B., 1996, ApJ, 473, L87  
 Deguchi S., Watson W.D., 1987, Phys. Rev. Letters, 59(24), 2814  
 Ebbels T., Ellis R., Kneib J.-P., Le Borgne J.-F., Pello R., Smail I., Sanahuja B., 1998, MNRAS, 295, 75  
 Esseen C.-G., 1942, Ark. Math. Astr. Fys. A, 28, 1  
 Fukuda S. et al., 2000, Phys.Rev.Lett, 85 (19), 3999  
 Gould A., 1995, ApJ, 455, 44  
 Gould A., 1996, ApJ, 470, 201  
 Hawkins M.R.S., 1996, MNRAS, 278, 787  
 Hu W., Eisenstein D., Tegmark M., 1998, Phys.Rev.Lett., 80, 5255  
 Jahreiss H., Wielen R., 1997, in B. Battrick, M.A.C. Perryman P.L. Bernacca, eds, *Hipparcos*, Venice '97: Presentation of the *Hipparcos* and Tycho Catalogues and First Astrophysical Results of the *Hipparcos* Space Astrometry Mission, ESA SP-402, Noordwijk, ESA, p.675  
 Kayser R., Refsdal S., Stabell R., 1986, A&A, 166, 36  
 Kneib J.-P., Mellier Y., Fort B., Mathez G., 1993, A&A, 273, 367  
 Kneib J.-P., Ellis R.S., Smail I., Couch W.J., Sharples R.M., 1996, ApJ, 471, 643  
 Lahav O., Liddle A.R., 2003, hep-ph/0309040  
 Lasserre T. et al., 2000, A&A, 355, L39  
 Lewis G.F., Ibata R.A., 2001, ApJ, 549, 46  
 Lewis G.F., Ibata R.A., Wyithe J.S.B., 2000, ApJ, 542, L9  
 Liebes S., 1964, Phys.Rev., 133(3B), 835  
 Metcalfe L. et al., 2003, A&A, 407, 791  
 Muños C., 2003, hep-ph/0309346  
 Neindorf B., 2003, A&A, 404, 83  
 Paczyński B., 1986, ApJ, 301, 2  
 Pello R., Schaefer D., Richard J., Le Borgne J.-F., Kneib J.-P., A&A, 2004, 416, L35  
 Refsdal S., Stabell R., 1991, A&A, 250, 62  
 Refsdal S., Stabell R., 1997, A&A, 325, 877  
 Riffeser A. et al., 2001, A&A, 379, 362  
 Sadoulet B., 1999, Rv.M.P., 71 (2), 197  
 Sarajedini V.L., Gilliland R.L., Phillips M.M., 2000, AJ, 120, 2825  
 Schechter P.L., Wambsganss J., 2002, ApJ, 580, 685  
 Schechter P.L. et al., 2003, ApJ, 584, 657  
 Schneider P., 1984, A&A, 140, 119  
 Schneider P., Ehlers J., Falco E.E., 1992, Gravitational lenses, Springer  
 Seitz C., Schneider P., 1994, A&A, 288, 1  
 Seitz C., Wambsganss J., Schneider P., 1994, A&A, 288, 19  
 Smail I., Dressler A., Kneib J.-P., Ellis R.S., Couch W.J., Sharples R.M., Oemler A.Jr., 1996, ApJ, 469, 508  
 Tadros H., Warren S., Hewett P., 1998, NewA Rev., 42, 115  
 Totani T., 2003, ApJ, 586, 735  
 Udalski A., Kubiak M., Szymanski M., 1997, Acta Astronomica, 47, 319  
 Walker M.A., Ireland P.M., 1995, MNRAS, 275, L41  
 Zackrisson E., Bergvall N., Marquart T., Helbig P., 2003, A&A, 408, 17

## APPENDIX A: DERIVATION OF FORMULA (30)

The derivation presented here follows very closely the lines of that by Neindorf (2003). We do not include all the steps of this derivation which can be found in the original work.<sup>5</sup>

Starting with the expression for the magnification factor (27) one has the following result for the observed flux of a source with surface profile  $I'(\zeta - \zeta_o) = I_o/(\pi R^2) \times \Theta(R - |\zeta - \zeta_o|)$  placed at  $\zeta_o$ :

$$I(\zeta_o) = \frac{1}{|1 - \kappa_c|^2} \int_{\mathcal{S} \times \mathcal{L}} d^2\zeta d^2\mathbf{z} I'(\zeta - \zeta_o) \delta(\zeta - \hat{J}_o \mathbf{z} + \mathbf{S}(\mathbf{z})) \quad (A1)$$

Its average value over  $\mathbf{S}(\mathbf{z})$  is well-known to be independent of microlensing population mass distribution and source profile (see, e.g. Schneider, Ehlers & Falco 1992, Chapter 11)

$$\begin{aligned} \langle I \rangle &= \frac{I_o}{[1 - \kappa_c]^2 [(1 - \kappa)^2 - \gamma^2]} \\ &= \frac{I_o}{|1 - \kappa_c|^2 |\det \hat{J}|} \end{aligned} \quad (A2)$$

where  $\hat{J} \equiv \hat{J}_o - \kappa \hat{1}$ .

The value of  $I^2(\zeta_o)$  is calculated in a similar manner:

$$\begin{aligned} I^2(\zeta_o) &= \frac{1}{|1 - \kappa_c|^4} \int_{\mathcal{S}^2} d^2\zeta_1 d^2\zeta_2 I'(\zeta_1 - \zeta_o) I'(\zeta_2 - \zeta_o) \times \\ &\quad \int_{\mathcal{L}^2} d^2\mathbf{z}_1 d^2\mathbf{z}_2 \delta(\zeta_1 - \hat{J}_o \mathbf{z}_1 + \mathbf{S}_1) \delta(\zeta_2 - \hat{J}_o \mathbf{z}_2 + \mathbf{S}_2) \end{aligned} \quad (A3)$$

<sup>5</sup> Please note, however, that the asymptotes for the involved functions found here differ slightly from those found in (Neindorf 2003) due to some numerical error and a typo in the latter work.

where  $\mathbf{S}_1 = \mathbf{S}(z_1)$ ,  $\mathbf{S}_1 = \mathbf{S}(z_1)$ . Introducing the joint probability function density of  $\mathbf{S}_1$  and  $\mathbf{S}_2$   $\varphi(\mathbf{S}_1, \mathbf{S}_2, \mathbf{z}_1, \mathbf{z}_2)$  we can calculate the average value of  $I^2$ :

$$\langle I^2 \rangle = \frac{1}{|1 - \kappa_c|^4} \int_{\mathcal{S}^2 \times \mathcal{L}^2 \times \mathcal{R}^4} d^2\zeta_1 d^2\zeta_2 d^2\mathbf{z}_1 d^2\mathbf{z}_2 d^2\mathbf{S}_1 d^2\mathbf{S}_2 \quad (\text{A4})$$

$$\delta(\zeta_1 - \hat{J}_o \mathbf{z}_1 + \mathbf{S}_1) \delta(\zeta_2 - \hat{J}_o \mathbf{z}_2 + \mathbf{S}_2) \times$$

$$\varphi(\mathbf{S}_1, \mathbf{S}_2, \mathbf{z}_1, \mathbf{z}_2) I'(\zeta_1) I'(\zeta_2)$$

Changing to the Fourier domain and making use of  $\delta$ -functions we get:

$$\langle I^2 \rangle = \frac{1}{(2\pi)^4 |1 - \kappa_c|^4} \int_{\mathcal{R}^2 \times \mathcal{L}^2} d^2\tau_1 d^2\tau_2 d^2\mathbf{z}_1 d^2\mathbf{z}_2 \quad (\text{A5})$$

$$\tilde{I}(\tau_1) \tilde{I}(\tau_2) Q_2(\tau_1, \mathbf{z}_1, \tau_2, \mathbf{z}_2) e^{-i(\tau_1 \hat{J}_o \mathbf{z}_1 + \tau_2 \hat{J}_o \mathbf{z}_2)},$$

where

$$Q_2(\tau_1, \mathbf{z}_1, \tau_2, \mathbf{z}_2) \equiv \int_{\mathcal{R}^4} d^2\mathbf{S}_1 d^2\mathbf{S}_2 \varphi(\mathbf{S}_1, \mathbf{S}_2, \mathbf{z}_1, \mathbf{z}_2) e^{i(\tau_1 \mathbf{S}_1 + \tau_2 \mathbf{S}_2)} \quad (\text{A6})$$

is the Fourier transform, or characteristic function, of  $\varphi(\mathbf{S}_1, \mathbf{S}_2, \mathbf{z}_1, \mathbf{z}_2)$  and  $\tilde{I}(\tau)$  is the one of the source profile, which is the following for a uniformly radiating disc of radius  $R$  emitting a total flux  $I_o$ :

$$\tilde{I}(\tau) = \frac{2I_o}{R\tau} J_1(R\tau) \quad (\text{A7})$$

We introduce central and relative coordinates  $\tau_1 = \mathbf{T} - \mathbf{t}/2$ ,  $\tau_2 = \mathbf{T} + \mathbf{t}/2$ ,  $\mathbf{z}_1 = \mathbf{R}_c - \mathbf{r}/2$ ,  $\mathbf{z}_2 = \mathbf{R}_c + \mathbf{r}/2$ , assume that lens positions are not correlated and take the limit of an infinite lens plane to obtain the following expression ( $\hat{J}_o^T = \hat{J}_o$ ):

$$\langle I^2 \rangle = \frac{1}{(4\pi)^2 |1 - \kappa_c|^4} \frac{1}{|\det \hat{J}|} \times \quad (\text{A8})$$

$$\int d^2\mathbf{t} d^2\mathbf{r} \tilde{I}\left(-\frac{\mathbf{t}}{2}\right) \tilde{I}\left(\frac{\mathbf{t}}{2}\right) Q(\mathbf{t}, \mathbf{r}) e^{-\frac{i}{2}(\hat{J}_o^T \mathbf{t}) \mathbf{r}},$$

where the  $\delta$ -functions in  $\mathbf{R}_c$  and  $\mathbf{T}$  have been utilized and for

$$Q(\mathbf{t}, \mathbf{r}) \equiv Q_2\left(-\frac{\mathbf{t}}{2}, -\frac{\mathbf{r}}{2}, \frac{\mathbf{t}}{2}, \frac{\mathbf{r}}{2}\right)$$

the following expression was obtained (Neindorf 2003)

$$Q(\mathbf{t}, \mathbf{r}) = e^{-\frac{n}{2}r^2 a(s)}. \quad (\text{A9})$$

Here  $s = \frac{t}{r}$  and the angle  $\chi$  between  $\mathbf{s}$  and positive  $Ox$  ray equals the angle between  $\mathbf{t}$  and  $\mathbf{r}$ . Function  $a(s, \chi)$  is the mass average of  $\alpha(ms, \chi)$

$$a(s, \chi) \equiv \int dm \phi(m) \alpha(ms, \chi),$$

the latter given by

$$\alpha(s, \chi) \equiv \int_{-\infty}^{\infty} dx \frac{1 - e^{isx}}{x^2} f(x, \chi) \quad (\text{A10})$$

Finally, the function  $f(x, \chi)$  is defined as

$$f(x, \chi) \equiv \quad (\text{A11})$$

$$\int_{-\pi/2}^{\pi/2} \frac{\cos^2 \phi d\phi}{\sqrt{(x - 2 \cos \chi)^2 \cos^2 \phi + (x \sin \phi + 2 \sin \chi \cos \phi)^2}}$$

and can be expressed analytically in terms of complete elliptic integrals:

$$f(x, \chi) = \frac{1}{u+1} \left\{ \left[ 1 + \frac{1 - x \cos \chi}{u} \right] K(v) + \frac{(1 - x \cos \chi)(1+u)^2}{2u^2} [E(v) - K(v)] \right\} \quad (\text{A12})$$

with  $u = \sqrt{x^2 - 2x \cos \chi + 1}$  and  $v = 4u/(u+1)^2$ .

The function  $\alpha(s, \chi)$  is therefore easily computed numerically. However, its overall behaviour is easily guessed from the following two analytic asymptotes:

$$\alpha(s, \chi) \xrightarrow{s \rightarrow \infty} \pi s - i \frac{\pi}{2} \cos \chi \quad (\text{A13})$$

valid to the accuracy of  $\sim 1$  per cent at  $s \geq 3 - 5$  and

$$\alpha(s, \chi) \xrightarrow{s \rightarrow 0} \frac{\pi}{2} s^2 \left( \frac{1}{2} + 2 \ln 2 - \tilde{\gamma} + \cos^2 \chi - \ln s \right) \quad (\text{A14})$$

$$- i \pi s \cos \chi$$

$$\approx \frac{\pi}{2} s^2 (1.3 + \cos^2 \chi - \ln s) - i \pi \cos \chi$$

where  $\tilde{\gamma} \equiv \lim_{n \rightarrow \infty} (\sum_{k=1}^n 1/k - \ln n) \approx 0.577216$  is Euler's constant.

Substituting the expression (A7) for  $\tilde{I}(\tau)$  into (A8), expanding

$$-\frac{i}{2}(\hat{J}_o^T \mathbf{t}) \mathbf{r} = -\frac{i}{2}rt[\cos \chi + \gamma \cos(\chi + 2\alpha_r)]$$

and using the change of variables  $\mathbf{t} = r\mathbf{s}$  we can immediately integrate over the angular component  $\alpha_r$  of  $\mathbf{r}$  to get

$$\langle I^2 \rangle = \frac{2I_o^2}{\pi |1 - \kappa_c|^4 |\det \hat{J}| R^2} \times \quad (\text{A15})$$

$$\int_0^\infty dr \int_0^\infty ds \int_0^{2\pi} d\chi \frac{r}{s} J_1^2\left(R \frac{rs}{2}\right) J_0\left(\gamma \frac{r^2 s}{2}\right) e^{-\frac{r^2}{2}[na(s, \chi) + is \cos \chi]}$$

Thus, using expression (A2) for the average value of observed flux we obtain the integral (30).

## APPENDIX B: EVALUATION OF INTEGRAL (32)

To evaluate the integral in (32) we consider the asymptotes of  $B(\sigma, \chi)$  which follow directly from the asymptotes (A14, A13) of the function  $\alpha(\sigma, \chi)$  introduced in the Appendix A:

$$B(\sigma, \chi) \approx \frac{\kappa}{2} m_{\text{eff}} \sigma (1.3 + \cos^2 \chi - \frac{\langle m^2 \ln m \rangle}{\langle m^2 \rangle} - \ln \sigma) \quad (\text{B1})$$

$$+ i(1 - \kappa) \cos \chi, \quad \sigma \ll 1$$

$$B(\sigma, \chi) \approx B(\chi) = \kappa + i \cos \chi, \quad \sigma \gg 1 \quad (\text{B2})$$

with  $m_{\text{eff}} = \langle m^2 \rangle / \langle m \rangle$  (Refsdal & Stabell 1991).

At  $\gamma \geq 10^{-2}$  it is convenient to split the integration over  $s$  into the following five regions:

- (i)  $0 \leq s \leq \sigma_1 R^2 / 2$ ,  $\sigma_1 \ll 1$
- (ii)  $\sigma_1 R^2 / 2 \leq s \leq \sigma_2 R^2 / 2$ ,  $\sigma_2 \gg 1$

- (iii)  $\sigma_2 R^2/2 \leq s \leq \sigma_3 \gamma^2$ ,  $\sigma_3 \ll 1$
- (iv)  $\sigma_3 \gamma^2 \leq s \leq \sigma_4$ ,  $\sigma_4 \gg 1$
- (v)  $\sigma_4 \leq s$

Due to the assumptions on  $\gamma$  and  $R$  made, in regions (i – iii) the convergence of the integral in  $\rho$  is provided by  $J_0(\gamma\rho)$  and  $e^{-B\rho}$  while  $J_1^2(\sqrt{s\rho}) \approx s\rho/4$  holds well for all values of  $\rho$  where the integrand is any significant. Therefore

$$\begin{aligned} \int_0^\infty d\rho J_1^2(\sqrt{s\rho}) J_0(\gamma\rho) e^{-\rho B} &\approx \frac{s}{4} \int_0^\infty d\rho \rho J_0(\gamma\rho) e^{-\rho B} \\ &= \frac{s}{4} \frac{B}{(B^2 + \gamma^2)^{3/2}}. \end{aligned} \quad (\text{B3})$$

In addition, in regions (i) and (iii) approximations (B1) and (B2) can be used, respectively. The latter approximation is even better in regions (iv) and (v) but (B3) clearly fails there. Let us consider the five regions in turn:

$$1. 0 \leq s \leq \sigma_1 \frac{R^2}{2}$$

Returning to the variable  $\sigma = 2s/R^2$  we can write down this part of the integral as follows:

$$I_1 = \frac{1}{4} \int_0^{\sigma_1} \frac{d\sigma}{\sigma} \int_0^{2\pi} \frac{B(\sigma, \chi) d\chi}{[B^2(\sigma, \chi) + \gamma^2]^{3/2}}. \quad (\text{B4})$$

We can rewrite  $B$  of (B1) in the following form:

$$B(\sigma, \chi) = |1 - \kappa|(x \pm i \cos \chi), \quad (\text{B5})$$

where

$$x \equiv \frac{\kappa}{2} \frac{m_{\text{eff}}}{|1 - \kappa|} (1.3 + \cos^2 \chi - \frac{\langle m^2 \ln m \rangle}{\langle m^2 \rangle} - \ln \sigma) \sigma \quad (\text{B6})$$

and at sufficiently small  $\sigma$  when the logarithm term dominates  $x$  is nearly independent of  $\chi$ . Then

$$I_1 = \frac{1}{4} \int_0^{\sigma_1} \frac{d\sigma}{\sigma} \frac{1}{|1 - \kappa|^2} g_1 \left( x(\sigma), \frac{\gamma}{|1 - \kappa|} \right), \quad (\text{B7})$$

where

$$g_1(x, \delta) \equiv 2 \int_0^\pi \frac{(x + i \cos \chi) d\chi}{[\delta^2 + (x + i \cos \chi)^2]^{3/2}}. \quad (\text{B8})$$

We have found numerically that the following approximation holds for  $g_1(x, \delta)$  with an accuracy of  $\leq 1$  per cent:

$$g_1(x, \delta) \simeq \frac{g_1(|1 - \delta|, \delta)}{|1 - \delta|} x, \quad x \leq x_{\text{max}} = |1 - \delta| \quad (\text{B9})$$

$x_{\text{max}}$  stands for the point where  $g_1$  reaches its maximum at a given  $\delta$ . This maximum value is approximately  $|1 - \delta|^{-1}$  for  $|1 - \delta| \leq 10^{-2}$  and should be calculated directly otherwise.

At  $|1 - \delta| > \sigma_1 \ln \sigma_1$  we can therefore perform an integration over  $\sigma$  in (B7) to get

$$\begin{aligned} I_1 &= \frac{1}{4} \frac{\kappa m_{\text{eff}}}{2|1 - \kappa|^2} \frac{g_1 \left( \left| 1 - \frac{\gamma}{|1 - \kappa|} \right|, \frac{\gamma}{|1 - \kappa|} \right)}{|1 - \kappa| - \gamma} \times \\ &\quad \left( 1.8 - \frac{\langle m^2 \ln m \rangle}{\langle m^2 \rangle} + \ln \frac{e}{\sigma_1} \right) \sigma_1. \end{aligned} \quad (\text{B10})$$

When  $\sigma_1$  does not obey the condition just formulated,

we just replace it with  $\sigma'_1 < \sigma_1$  such that  $\sigma'_1 \ln \sigma'_1$  is smaller than  $|1 - \gamma|/|1 - \kappa|$  and move the rest of the calculations to region (ii) where it is performed numerically.

The problem arises with  $|1 - \delta| \rightarrow 0$  but this corresponds to the case of diverging average amplification and the microlensing-induced variability is expected to drop logarithmically to zero in this case (Deguchi & Watson 1987). Formally, it does happen in our calculations -  $\det \hat{J}$  in front of the integral (32) make it go to zero linearly in all regions but (i) where the ratio of the determinant and denominator of (B10) tends to a non-zero limit, while  $g_1 \sigma'_1 \ln \sigma'_1$  provides the behaviour expected. However, numerical calculations become unreliable in this case and so we do not calculate  $\varepsilon_\mu^2$  for  $(\kappa, \gamma)$  closer than approximately 0.03 to the  $\gamma = |1 - \kappa|$  lines in  $\kappa\gamma$  plane.

Another apparent problem with (B10) seems to be present when  $\kappa \rightarrow 1$ , but this turns out to be a slight technical issue with no real computational consequences and therefore may be called ‘a removable discontinuity’.

$$2. \sigma_1 R^2/2 \leq s \leq \sigma_2 R^2/2$$

This region is the easiest to compute:

$$I_2 = \frac{1}{4} \int_{\sigma'_1}^{\sigma_2} \frac{d\sigma}{\sigma} g_2(\sigma). \quad (\text{B11})$$

where

$$g_2(\sigma) \equiv \int_0^{2\pi} \frac{B(\sigma, \chi) d\chi}{[B^2(\sigma, \chi) + \gamma^2]^{3/2}} \quad (\text{B12})$$

and  $B(\sigma, \chi)$  is computed numerically by interpolation of  $\alpha(\sigma, \chi)$  which is computed in advance with good accuracy.

The computations of  $I_2$  provide no problem from either conceptual or computational point of view but it transpires that they are the most time consuming part of the procedure.

$$3. \sigma_2 R^2/2 \leq s \leq \sigma_3 \gamma^2$$

At  $s \geq \sigma_2 R^2/2$  the function  $B(2s/R^2, \chi) = \kappa + i \cos \chi$  to high accuracy and does not depend on  $s$ . Therefore the integral over  $\chi$ :

$$g_3(\kappa, \gamma) \equiv \int_0^{2\pi} \frac{(\kappa + i \cos \chi) d\chi}{[(\kappa + i \cos \chi)^2 + \gamma^2]^{3/2}} \quad (\text{B13})$$

(which equals  $g_1$  introduced above for  $x = \kappa$  and  $\delta = \gamma$ ) turns out to be a common factor and the integral with respect to  $s$  is elementary:

$$I_3 = \frac{1}{4} g_3(\kappa, \gamma) \ln \frac{2\sigma_3 \gamma^2}{\sigma_2 R^2} \quad (\text{B14})$$

$$4 \& 5. s > \sigma_3 \gamma^2$$

In regions (iv) and (v) the approximation (B2) is still valid, therefore

$$I_4 + I_5 = \int_{\sigma_3 \gamma^2}^\infty \frac{ds}{s^2} \int_0^\infty d\rho J_1^2(\sqrt{s\rho}) J_0(\gamma\rho) \times \quad (\text{B15})$$

$$\int_0^{2\pi} d\chi e^{-\rho(\kappa+i\cos\chi)} = 2\pi \int_{\sigma_3\gamma^2}^{\infty} \frac{ds}{s^2} g_4(s, \kappa, \gamma),$$

where

$$g_4(s, \kappa, \gamma) \equiv \int_0^{\infty} d\rho J_1^2(\sqrt{s\rho}) J_0(\gamma\rho) J_0(\rho) e^{-\kappa\rho}. \quad (\text{B16})$$

The integrand in  $g_4$  decreases exponentially and therefore it is sufficient to perform a numerical integration up to some  $\rho_{max}/\kappa$ . The absolute value of the residual can be easily estimated

$$R = \left| \int_{\frac{\rho_{max}}{\kappa}}^{\infty} d\rho J_1^2(\sqrt{s\rho}) J_0(\gamma\rho) J_0(\rho) e^{-\kappa\rho} \right| \leq \int_{\frac{\rho_{max}}{\kappa}}^{\infty} d\rho e^{-\kappa\rho} = \frac{1}{\kappa} e^{-\rho_{max}}. \quad (\text{B17})$$

The value  $\rho_{max} \sim 30$  turned out to be suitable for all our purposes.

For completeness we can write down the integration in region (iv), which is done numerically:

$$I_4 = 2\pi \int_{\sigma_3\gamma^2}^{\sigma_4} \frac{ds}{s^2} g_4(s, \kappa, \gamma). \quad (\text{B18})$$

The integration in region (v) is accomplished by considering the asymptotic behaviour of  $g_4$  at large  $s$ . The integral (B16) effectively splits into two - with  $\rho \leq \rho_o/s$  and  $\rho \geq \rho_o/s$  with  $\rho_o \sim 1$ . Invoking the asymptotics of Bessel functions one can see that the second of these integrals is proportional to  $1/\sqrt{s}$  and represents a leading term when  $s \rightarrow \infty$ . Using the asymptotic formula  $J_1(x) \simeq \sqrt{2/(\pi x)} \cos(\pi x/2 + \alpha)$  and noting that the cos-term oscillates rapidly for  $x \gg 1$  we find the following limiting value for  $g_4$ :

$$g_4(s, \kappa, \gamma) \rightarrow \frac{1}{\pi\sqrt{s}} g_5(\kappa, \gamma),$$

where

$$g_5(\kappa, \gamma) \equiv \int_0^{\infty} \frac{d\rho}{\sqrt{\rho}} J_0(\rho) J_0(\gamma\rho) e^{-\kappa\rho}. \quad (\text{B19})$$

This integration is again done only up to some  $\rho_{max}/\kappa$ .

Thus we obtain the last portion needed to compute  $\epsilon_{\mu}^2$ :

$$I_5 = 2\pi \int_{\sigma_4}^{\infty} \frac{ds}{s^2} g_4(s, \kappa, \gamma) \approx \frac{4}{3} \frac{g_5(\kappa, \gamma)}{\sigma_4^{3/2}}. \quad (\text{B20})$$

Putting all the pieces together we may now write the result:

$$\epsilon_{\mu}^2(\kappa, \gamma, R) + 1 = \frac{|\det \tilde{J}|}{\pi} \left[ I(\kappa, \gamma) - \frac{g_3(\kappa, \gamma)}{2} \ln R \right], \quad (\text{B21})$$

where

$$I(\kappa, \gamma) \equiv I_1 + I_2 + I_4 + I_5 + \frac{g_3(\kappa, \gamma)}{4} \ln \frac{2\sigma_3\gamma^2}{\sigma_2}. \quad (\text{B22})$$

We should note here that it is exactly the behaviour of  $J_1(\sqrt{s\rho})$  - namely the possibility to approximate it

with  $\sqrt{s\rho}/2$  - in the whole region of actual dependence of  $B(2s/R^2, \chi)$  on  $s$  that makes the result virtually independent of  $R$  allowing it to appear in region (iii) only.

Considering the constants  $\sigma_i$  used in the actual calculations we found that the following values provide the best compromise between the accuracy of the computations and the time needed to perform them:  $\sigma_1 = 0.03$ ,  $\sigma_2 = 4$ ,  $\sigma_3 = 0.03$ ,  $\sigma_4 = 30$ . This corresponds to the case when  $\phi(m) = \delta(m-1)$  which is the case actually considered. We have checked that changes in these constants do not affect the results.